Sea surface kinematics from near-nadir radar measurements

Frédéric Nouguier, Bertrand Chapron, Fabrice Collard
Alexis Mouche, Nicolas Rascle, Fabrice Ardhuin and Xiaoqing Wu

***Abstract*—Doppler radars at all incidence angles measure mean velocities and spread that have complex relations to oceanic motions, with opportunities to measure winds, waves and currents. Here we extend previous theoretical models of backscatter and Doppler using a Kirchhoff approximation and physical optics model. We show that in Ka-band, around 12° incidence, range-resolved measurements of Doppler and backscatter provide unambiguous estimations of the wave spectrum and surface current. This property is illustrated with numerical examples and airborne data from the AirSWOT instrument. The same measurement conditions can be exploited for global ocean mapping from low Earth orbit sensor satellite configuration.**

***Index Terms*—Microwave remote sensing, Doppler, current, SWOT, surface kinematics multiscale (SKIM) concept.**

I. INTRODUCTION

DOPPLER frequency anomalies, i.e. the difference between the measured and the geometrically predicted Doppler frequencies, can provide local instantaneous line-of-sight surface velocities from airborne and satellite-borne radar measurements over ocean scenes [1], [2], [3]. These velocities are governed by the distributed dispersion of the detected ocean surface wave scatterers, and thus linked to the properties of local waves [4], [5], and current [6], [7].

Doppler anomalies thus provide direct ocean surface velocity measurements from space, possibly performing better than altimetry for small scale currents, as neither a gradient of the measured quantity, nor a relationship between sea level and current is assumed.

Yet, sensor physics and optimal instrumental configurations (incidence angle, wavelength, polarization) are still to be clarified for the analysis of present measurements and the design of future satellite missions [8]. Indeed, these direct surface velocity measurements relate to detected scatter motions including both orbital and surface current velocity. With that goal in mind, we consider here the particular case of a near-nadir configuration for a radar instrument operating at high frequency (Ka-band). In that case, the Kirchhoff asymptotic electromagnetic model framework is sufficient [2], [9]. A key point is that a Kirchhoff integral operates as an harmonic filter at a selected resonant directional wavenumber $\boldsymbol{Q_H}$ of the joint characteristic function of the random surface elevations. This property follows from invariance by translation of the scattering cross section. It ensues that a zero-mean time varying sea surface produces measurable phase shifts directly associated to the time derivative of this joint characteristic function. Under near Gaussian statistics, the phase shifts are functions of moments of the surface elevation spectrum.

As derived in section 2, asymptotic analytical solutions provide the expected statistical properties of both the normalized radar cross section and its associated Doppler frequency. These developments are further discussed in section 3 for radar measurements highly-resolved in the range direction. In such a real-aperture-radar (RAR) imaging configuration, time-varying complex reflectivity modulations emerge, depending on the range-resolved ocean wave direction. Combined to mean complex reflectivity measurements dominated by wind-dependent short waves, this gives a quantitative knowledge of the ambient sea state conditions. Namely, long wave directional spectral properties and kinematics. The present developments extend previous analysis [10], [11], [12] to time-varying ocean surfaces. Combined range-resolved radar cross-section and Doppler anomalies further open new strategies to separate wave induced motions and surface current. Analytical solutions are then compared to near-nadir, highly-resolved, Ka-band Doppler airborne measurements in section 4. Conclusions follow in section 5.

II. SCATTERING MODEL AND DOPPLER EVALUATION

A. Basic equations

The co-variance of scattered fields (e.g. [2], [13]) is expressed as

$$C(\tau) = \langle \boldsymbol{E}(\boldsymbol{K}, t)\boldsymbol{E}^*(\boldsymbol{K}, t+\tau)\rangle \tag{1}$$

with τ the time lag, and $\boldsymbol{K}$ the electromagnetic wavenumber. The $\langle . \rangle$ operator represents a spatial averaging and the star superscript stands for the complex conjugate. For near nadir geometry and sufficiently high electromagnetic microwave frequency, i.e. Ku- or Ka-band, polarization effects can be ignored, and the Kirchhoff Approximation (KA) provides adequate scattering asymptotic solutions.

Denoting $\boldsymbol{K}_0$ and $\boldsymbol{K}$, the incident and scattered EM wave vectors, with their respective horizontal $\boldsymbol{k}_0$, $\boldsymbol{k}$ and vertical $-q_0$, q components, one has

$$\boldsymbol{K}_0 = \boldsymbol{k}_0 - q_0\hat{\boldsymbol{z}}, \qquad \boldsymbol{K} = \boldsymbol{k} + q\hat{\boldsymbol{z}}, \tag{2}$$

with positive q and q_0 given by $k_0^2 + q_0^2 = k^2 + q^2 = K_0^2$. The Ewald vector is defined as $\boldsymbol{Q} = \boldsymbol{K} - \boldsymbol{K}_0$ with horizontal $\boldsymbol{Q_H} = \boldsymbol{k} - \boldsymbol{k_0}$ and vertical $Q_z = q + q_0$ components.

F. Nouguier, B. Chapron, A. Mouche, N. Rascle and F. Ardhuin are with the Laboratoire d'Océanographie Physique et Spatiale, Univ. Brest, CNRS, Ifremer, IRD,29200 Plouzané, France e-mail: frederic.nouguier@ifremer.fr, F. Collard is with the OceanDataLab, Locmaria-Plouzané and X. Wu is with the Jet Propulsion Laboratory, California Institute of Technology, NASA

Manuscript received June 6, 2017.

Under KA, the electric scattered field writes $\boldsymbol{E}_{KA} = -\mathrm{i}\mathrm{e}^{\mathrm{i}KR}\boldsymbol{E}_0\mathbb{S}(\boldsymbol{K})/R$ where $\boldsymbol{E}_0$ is the incident field amplitude, R the distance between the satellite and the ground beam center and $\mathbb{S}$ the scattering matrix

$$\mathbb{S}(\boldsymbol{K},t) = \frac{\mathcal{K}}{Q_z(2\pi)^2}\int_A \mathbf{d}\boldsymbol{r}\ \mathrm{e}^{\mathrm{i}\boldsymbol{Q_H}\cdot\boldsymbol{r}}\ \mathrm{e}^{\mathrm{i}Q_z\eta(\boldsymbol{r},t)} \quad (3)$$

with A the illuminated area at time t, $\mathcal{K}$ the Kirchhoff kernel and η the sea surface elevation. Equation (1) then writes

$$C(\tau) \propto \iint_{A,A} \mathrm{e}^{\mathrm{i}\boldsymbol{Q_H}\cdot(\boldsymbol{r}-\boldsymbol{r'})}\langle \mathrm{e}^{\mathrm{i}Q_z(\eta(\boldsymbol{r'},t+\tau)-\eta(\boldsymbol{r},t))}\rangle \mathrm{d}\boldsymbol{r}\mathrm{d}\boldsymbol{r'}. \quad (4)$$

B. Mean Doppler frequency

Assuming that the instrument motion relative to the solid Earth is accurately evaluated, the remaining mean geophysical Doppler (GD) frequency f_{GD}, can be defined as [3]

$$2\pi f_{GD} = -\mathrm{i}\partial_\tau C(0)/C(0) \quad (5)$$

where, from now on, ∂_α is the derivation relative to α variable, $\widehat{\boldsymbol{x}}$ is the ground range direction and $\widehat{\boldsymbol{y}}$ the ground azimuth direction, so that $\boldsymbol{Q_H} = Q_H\hat{\boldsymbol{x}}$. Considering $(\boldsymbol{r'}, t+\tau) = (\boldsymbol{r}+\boldsymbol{\xi}, t+\tau)$, and homogeneous Gaussian statistics for the sea surface elevation, Eq. (5) becomes

$$2\pi f_{GD} = -\mathrm{i}\partial_\tau\zeta^0/\zeta^0 \quad (6)$$

where

$$\zeta(\tau) = \int_A \mathrm{e}^{\mathrm{i}Q_H\xi_x}\mathrm{e}^{-Q_z^2(\rho(0,0)-\rho(\boldsymbol{\xi},\tau))}\mathrm{d}\boldsymbol{\xi}. \quad (7)$$

The range component of $\boldsymbol{\xi}$ is ξ_x, and ρ is the spatio-temporal surface elevation correlation function whose expression can be found in appendix VI-A. In (7), $\boldsymbol{Q}_H$ and Q_z dependency is implicit in the definition of ζ and the zero superscript corresponds to quantity taken at $\tau = 0$ as

$$\zeta^0 = \zeta(\boldsymbol{Q}_H,\ Q_z,\ 0) \quad \text{and} \quad \partial_\tau\zeta^0 = \left.\frac{\partial\zeta(\boldsymbol{Q}_H,\ Q_z,\tau)}{\partial\tau}\right|_{\tau=0}.$$

The correlation function can be expanded

$$\begin{aligned}\rho(\boldsymbol{\xi},\tau) &\simeq \rho(\boldsymbol{\xi},0) + \partial_t\rho(\boldsymbol{\xi},0)\tau & (8)\\ &\simeq \rho(\boldsymbol{\xi},0) + \mathbf{msv}\cdot\boldsymbol{\xi}\tau & (9)\end{aligned}$$

introducing the mean slope speed vector

$$\mathbf{msv} = (\mathrm{mss_{xt}}, \mathrm{mss_{yt}}) = \partial_\tau\boldsymbol{\nabla}_{\boldsymbol{\xi}}\rho(0,0). \quad (10)$$

with the definition of all mean squared quantities

$$\mathrm{mss}_{x^\alpha y^\beta t^\gamma} = 2\int_{\mathbb{R}^2} k_x^\alpha k_y^\beta \omega^\gamma S_\mathrm{d}(\boldsymbol{k})\ \mathrm{d}\boldsymbol{k} \quad (11)$$

from spectral moments of S_d, the directional (i.e. single-sided) ocean elevation spectrum (see appendix VI-A for details). Inserting (9) in (6) leads to

$$2\pi f_{GD} = Q_z^2\mathrm{mss_{xt}}\partial_{Q_H}\zeta^0/\zeta^0 \quad (12)$$

where the Q_H derivation has to be done at constant Q_z.

Following, the radar cross section writes

$$\sigma^0 = \frac{1}{\pi}\frac{|\mathcal{K}|^2}{(2K)^2}\sec^2(\theta)\zeta^0, \quad (13)$$

with θ being the incidence angle. The ζ^0 term brings an additional $\sec^2(\theta)$ dependency. To ease the development, let us introduce $\psi^0 = \cos^4(\theta)\sigma^0$. Note, in equation (12), the Q_H differentiation at constant Q_z can not be directly derived. However, at close nadir incidence, a $\cos(\theta)$ variation are small and we can simplify

$$\partial_{Q_H}|_{Q_z} \approx Q_z^{-1}\ \partial_{\tan\theta}|_K \quad (14)$$

giving,

$$f_{GD} = \frac{Q_z\mathrm{mss_{xt}}}{2\pi}\left(\frac{\partial_{\tan\theta}\psi^0}{\psi^0}\right). \quad (15)$$

It clearly highlights that the mean Doppler shift is directly linked to the rate of variation of the radar cross section with incidence. We note that for linear waves $\mathrm{mss_{xt}} = U_S^\infty/2$ where U_S^∞ is the surface Stokes drift velocity of deep water waves. For geophysical purposes, it is convenient to use the non-dimensional G factor introduced in [1],

$$G = 2\pi f_{GD}/Q_H U_S^\infty \approx \frac{1}{2\tan(\theta)}\left(\frac{\partial_{\tan\theta}\psi^0}{\psi^0}\right) \quad (16)$$

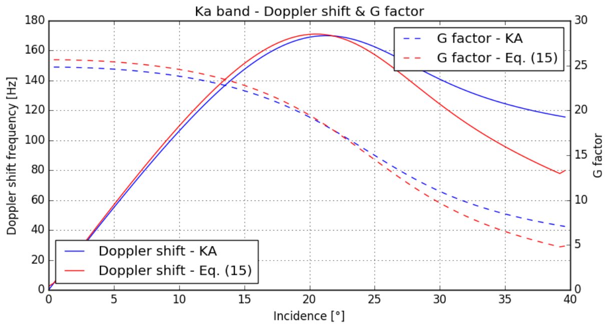

Fig. 1. Mean Doppler shift frequency versus incidence in upwind looking direction. 8 m/s wind speed Elfouhaily spectrum is considered at 20 km long fetch ($\lambda_{peak} \approx 45$ m). Solid blue curve is for Kirchhoff Assumption (KA) labeled eq. (12) and solid red curve for eq. (15). Dashed curves are the corresponding normalized factor G defined eq. (16)

Figure 1 shows the expected mean Ka-band Doppler shift frequency (left axis) and the G factor (right axis) versus incidence for a 20 km fetch upwind 8 $\mathrm{m.s^{-1}}$ wind speed Elfouhaily spectrum [14]. Close to nadir, up to about 20 degrees, equation (15) well approximate a full KA solution for the expected mean Doppler shift frequency.

In Ka-band radar data collected during the Southern Ocean Waves Experiment [15], the departure of the radar cross-section measurements from a Gaussian shape approximation was reported as

$$\ln\left(\frac{\cos^4(\theta)\sigma^0}{\sigma^0_\mathrm{max}}\right) = -A\tan^2(\theta) + B\tan^4(\theta). \quad (17)$$

Except for light wind speed, a robust relationship writes

$$B = 0.5676\ A^{1.332}. \quad (18)$$

The $\tan^2(\theta)$ rate of change A identifies with $1/\mathrm{mss_{shape}}$ as derived in [9] from Ka-band satellite measurements of the DPR on-board GPM. For wind speed of about 7 m/s with 1.5 m significant wave height, it gives

$$\left\{\begin{array}{ccl} A & = & \mathrm{mss}_{\mathrm{shape}}^{-1} \approx 33 \\ B & \approx & 60 \\ \left.\dfrac{\partial_{\tan\theta}\psi^0}{\psi^0}\right|_{\theta=12^\circ} & \approx & -11.7 \end{array}\right. \tag{19}$$

A typical upwind $\mathrm{mss}_{\mathrm{xt}}$ derived from a fully developed Elfouhaily spectrum at 7 m.s^{-1} wind speed is $\mathrm{mss}_{xt} \approx -0.054$ m.s^{-1}, leading to a Doppler shift frequency $f_{GD} \approx 155$ Hz at 12 degrees incidence. At this wind speed, the additional B term tends to decrease the $\partial_{\tan\theta}\psi^0/\psi^0$ term. A parabolic approximation of the $\cos^4(\theta)\sigma^0$ incidence fall-off would have then led to a 20% overestimation of the Doppler shift, i.e. about 30 Hz translating to a 12 cm.s^{-1} line-of-sight velocity difference.

C. Sea surface current Doppler shift

An additional horizontal current vector $\boldsymbol{U} = (U_x, U_y)$, vertically uniform with depth, modifies the surface wave dispersion

$$\omega = \sqrt{g|\boldsymbol{k}|(1 + |\boldsymbol{k}|^2/k_M^2)} + \boldsymbol{k}\cdot\boldsymbol{U} \tag{20}$$

where $\boldsymbol{k}$ is the wavenumber vector, and $k_M = 363.2$ rad.m^{-1}.

As shown in Appendix VI-A, the correlation function of the surface elevations simply becomes

$$\rho_c(\boldsymbol{\xi}, \tau) = \rho(\boldsymbol{\xi} - \boldsymbol{U}\tau, \tau) \tag{21}$$

Replacing (21) in (7), we now have

$$\zeta_c(\tau) = \mathrm{e}^{-\mathrm{i}Q_H U_x}\zeta(\tau) \tag{22}$$

$$f_C = \frac{Q_H}{2\pi}U_x = \frac{2\sin(\theta)}{\lambda_{em}}U_x \tag{23}$$

with λ_{em} being the electromagnetic wavelength ($\lambda_{em} \approx 8$ mm in Ka-band). In deriving the present asymptotic expression, the surface current contribution straightforwardly results from the modification of the wave dispersion relationship. Mathematically, the surface current modifies the wave vertical velocities $\partial_t\eta$, and thus appears trough the vertical Q_z factor in equation (7). This authorizes the change of variable (21) which acts to transform the modified vertical contribution onto an horizontal effect. Without change of variable and keeping the current impact on the vertical terms, the correlation function expansion (9) would be modified to also lead to equation (23).

At 12 degrees incidence, a 50 cm.s^{-1} horizontal current, in the radar looking direction, then corresponds to an additional 26 Hz Doppler shift. Compared to the expected large background Doppler bias, a stringent knowledge of the ambiant sea state condition in terms of both long waves and wind-dependent short waves, is thus an essential requisite for an accurate estimation of the current velocity.

III. RANGE RESOLVED MEASUREMENTS

To mitigate this difficulty, the dependency of Doppler and NRCS measurements on the sea state has first been expressed as a function of wind speed and direction [16], [17], [8]. Indeed, the wave-induced Doppler bias is dominated by wind-seas and largely minimized for cross-wind radar measurements to favor surface current estimates. Building on multiple azimuth and incidence angle observations, practical algorithms can be proposed [18]. Still, the expected root mean square variability of U_S^∞ for a given wind speed is 40% [5]. Hereafter, a complementary approach is exposed. It builds on range resolved measurements, to exploit detected radar signal modulations to more precisely characterize the ambient sea state conditions, especially providing an estimate of U_S^∞ that is more accurate that an empirical wind-based algorithm.

A. Modified basic equations

Resolution in the range (x) direction can be achieved by the convolution of the received and flipped emitted chirps, possibly leading to a fine resolution in the line of sight (e.g. 3 m projected on the ground for a 250 MHz bandwidth under satellite configuration). For each range gate, an estimation of (4) follows as

$$\widetilde{C}(x,\tau) \propto \iint_{A,A} \mathrm{e}^{\mathrm{i}\boldsymbol{Q_H}\cdot\boldsymbol{\xi}}\langle \mathrm{e}^{\mathrm{i}Q_z\eta_s' - \mathrm{i}Q_z\eta_s}\rangle \mathrm{e}^{\mathrm{i}Q_z(\eta_l'-\eta_l)} d\boldsymbol{r}d\boldsymbol{\xi} \tag{24}$$

The spatial integration is now performed over the resolved cell area A. Expansion in space and time gives

$$\eta_l'(\boldsymbol{r}+\boldsymbol{\xi}, t+\tau) = \eta_l + \boldsymbol{\nabla}\eta_l\cdot\boldsymbol{\xi} + \partial_t\eta_l\tau \tag{25}$$

yielding to

$$\begin{aligned} \widetilde{C}(x,\tau) \quad \propto \quad & \iint_{A,A} \mathrm{e}^{\mathrm{i}Q_z\partial_t\eta_l\tau + \mathrm{i}Q_z\boldsymbol{\nabla}\eta_l\cdot\boldsymbol{\xi}} d\boldsymbol{r} \\ & \times \mathrm{e}^{\mathrm{i}\boldsymbol{Q_H}\cdot\boldsymbol{\xi}}\langle \mathrm{e}^{\mathrm{i}Q_z(\eta_s'-\eta_s)}\rangle d\boldsymbol{\xi}. \end{aligned} \tag{26}$$

The intercepted area in the cross-line-of-sight or azimuth direction L_y is still very large, i.e. order of km, constrained by the antenna pattern. Assuming that $\partial_t\eta_l$ and $\boldsymbol{\nabla}\eta_l$ are Gaussian processes, evaluation of the along-azimuth integral in (26) leads to

$$A\exp\left[\mathrm{i}Q_z\overline{\partial_t\eta_l}(x)\tau + \mathrm{i}Q_z\overline{\partial_x\eta_l}(x)\xi_x\right] \times \langle \mathrm{e}^{\mathrm{i}Q_z(\eta_l'-\eta_l)}\rangle \tag{27}$$

where $\overline{\partial_t\eta_l}(x)$ and $\overline{\partial_x\eta_l}(x)$ are residual mean values of $\partial_t\eta_l$ and $\boldsymbol{\nabla}\eta_l$, respectively, integrated over the azimuth at a given x position (gate position) and implicit time t. Their expressions are not straightforward, given in appendix VI-B. To leading order, these residual mean azimuthal profiles, $\overline{\partial_t\eta_l}(x)$ and $\overline{\partial_x\eta_l}(x)$, depend on the azimuthal aperture, with residual variances increasing with their distributed azimuthal correlation lengths, and decreasing as L_y^{-1}. Note also, the cross-line-of-sight surface gradient has a much shorter correlation length in the azimuthal direction and its residual mean can be neglected, ie $\overline{\partial_y\eta_l}(x)$=0.

Inserting (27) in (26), and having again $\boldsymbol{Q_H} = Q_H\hat{\boldsymbol{x}}$, we find

$$\widetilde{C}(x,\tau) \quad \propto \quad A\mathrm{e}^{\mathrm{i}Q_z\overline{\partial_t\eta_l}(x)\tau} \times \widetilde{\zeta}(x,\tau) \tag{28}$$

where

$$\widetilde{\zeta}(x,\tau) = \int_A \mathrm{e}^{\mathrm{i}(Q_H + Q_z\overline{\partial_x\eta_l}(x))\xi_x} \mathrm{e}^{-Q_z^2(\rho(0,0)-\rho(\boldsymbol{\xi},\tau))} \mathrm{d}\xi_x \mathrm{d}\xi_y \tag{29}$$

recognized as the spatio-temporal Kirchhoff integral with an additional $Q_z\overline{\partial_x\eta_l}(x)$ phase term, correcting the initial resonant frequency Q_H. The range-resolved Doppler shift frequency then writes

$$2\pi f_{GD}(x) = -\mathrm{i}\frac{\partial_\tau \widetilde{C}(x,0)}{\widetilde{C}(x,0)} \tag{30}$$

B. NRCS and Doppler modulations

Range resolved measurements thus provide both the NRCS and Doppler at each gate. In particular, $\widetilde{\sigma}^0(x) \propto \sec^2(\theta)\widetilde{\zeta}^0(x)$, and assuming the overall tilting modulation by long waves in (29) to be sufficiently small, it simply comes

$$\widetilde{\psi}^0(x) = \psi^0 + \overline{\partial_x\eta_l}(x)\partial_{\tan\theta}\psi^0 \tag{31}$$

Using the same derivations as in section II-B, the resulting Doppler shift associated to a given gate, at distance x and time t, writes

$$2\pi f_{GD}(x) = Q_z\overline{\partial_t\eta_l} + Q_z\mathrm{mss_{xt}}\partial_{Q_H}\widetilde{\zeta}^0(x)/\widetilde{\zeta}^0(x) \tag{32}$$

and further approximated

$$\begin{aligned} 2\pi f_{GD}(x) \;\; = \;\; & Q_z\overline{\partial_t\eta_l}(x) + \qquad (33)\\ & \frac{Q_z\mathrm{mss_{xt}}}{\widetilde{\psi}^0(x)}\left[\partial_{\tan\theta}\psi^0 + \overline{\partial_x\eta_l}(x)\partial^2_{\tan^2\theta}\psi^0\right], \end{aligned}$$

where $\overline{\partial_t\eta_l}(x)$ and $\overline{\partial_x\eta_l}(x)$ are the space and time dependent mean azimuthal velocities and slopes of the long wave profile.

C. Numerical simulation

To illustrate these results, a numerical simulation is performed. A random Gaussian sea surface is simulated [19] and shown on figure 2. The surface is generated from Elfouhaily spectrum for a 20 km fetch 8 m.s^{-1} wind speed condition, leading to a wind sea system with a 45 m peak wavelength. Such a sea state corresponds to the environmental conditions discussed in the next section. A 5 meter ground resolution is assumed in the radar line of sight, in the upwind direction. The generated surface is sampled at a 2.5 m resolution. Mean azimuthal profiles of the surface slope in the range direction and the surface vertical velocities are shown figure 3. Azimuthal averaging is realized over 1280 m. NRCS as well as Doppler modulations are estimated through the full Kirchhoff Approximation (equation (30)) and the approximate equations (31) and (33). Figure (4) shows the Ka-band signal modulations at 12 degrees incidence. Very satisfying agreement between both methods is obtained. From now on, we use equation (31) for NRCS modulations and equation (33) for Doppler shift modulation.

Figure 5 compares expected NRCS modulation spectra obtained at 3,8 and 12 degrees incidence with the spectrum of the line-of-sight mean surface slope profile ($\overline{\partial_x\eta}$). As derived (31) and numerically obtained, NRCS modulation spectra

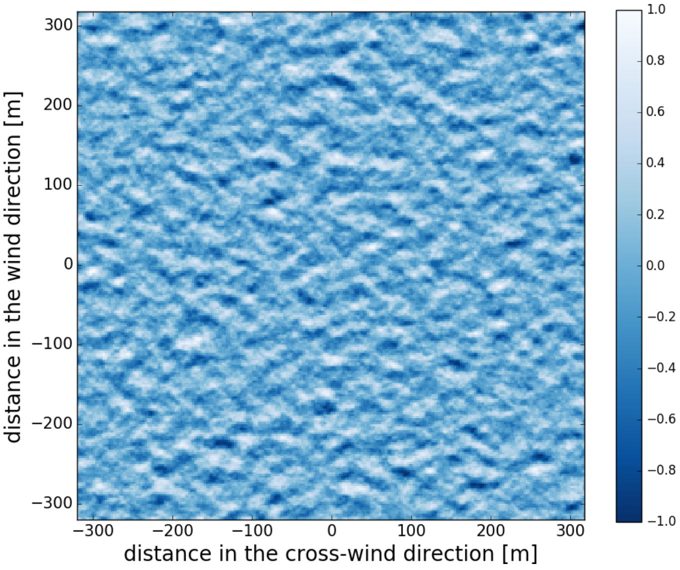

Fig. 2. A 640 m x 640 m patch extracted from a larger random 2560 m x 1280 m Gaussian sea surface. A 2.5 m sampling is used in both horizontal directions.

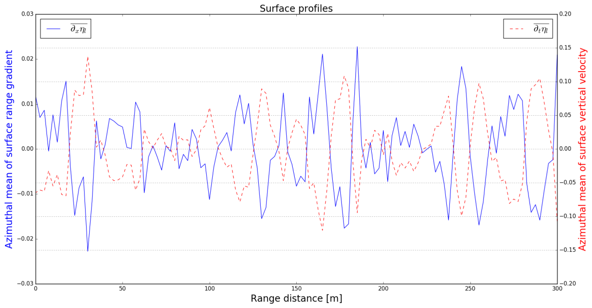

Fig. 3. Mean azimuthal profiles of the surface slope in the range direction and the surface vertical velocities. Averaging azimuthal length is 1280 m.

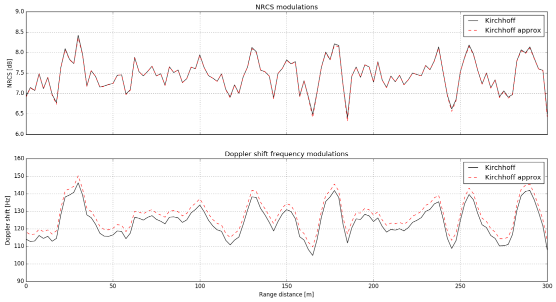

Fig. 4. Ka band NRCS and Doppler shift frequency range modulations versus range distance at a 12 degrees incidence radar. 8 m/s wind speed and 20 km long fetch Elfouhaily spectrum is considered. Solid curve is for Kirchhoff Assumption (KA) and dashed curves are for approximations (31) and (33)

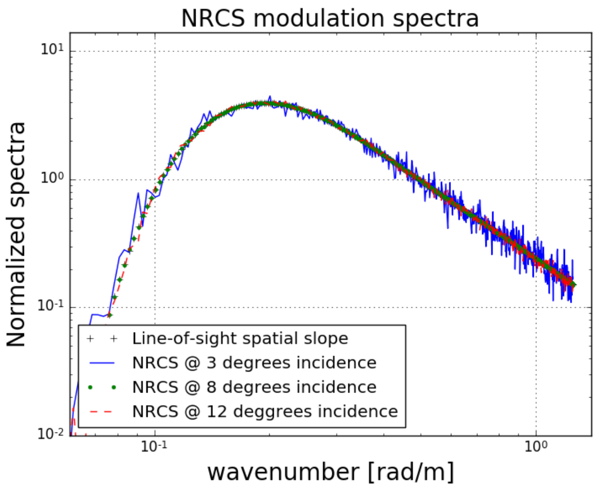

Fig. 5. Ka band - Normalized NRCS modulation spectra at 3, 8 and 12 degrees incidence. Line-of-sight sea surface slope ($\overline{\partial_x \eta}(x)$) spectra is also superimposed.

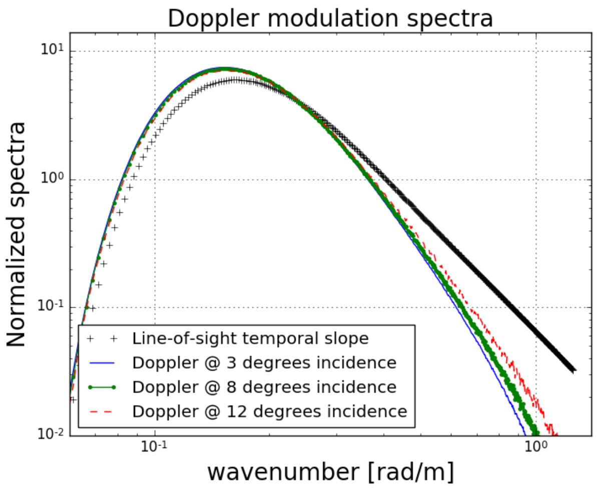

Fig. 6. Ka band - Normalized Doppler modulation spectra at 3, 8 and 12 degrees incidence. Line-of-sight sea surface temporal slope ($\overline{\partial_t \eta}(x)$) spectra is also superimposed.

are directly proportional to the surface line-of-sight slope spectrum. Such a principle is at the heart of the concept of the SWIM wave scatterometer on CFOSAT [20], [12]. To infer the full wave slope spectrum from the NRCS modulation spectrum, the determination of the Modulation Transfer Function (MTF) $\partial_{\tan\theta}\psi^0$ at each considered incidence and azimuth is necessary.

Figures 6 and 7 present modulation spectra of the range-resolved Doppler shifts, equation (33), and the weighted range-resolved Doppler shifts, i.e. $\widetilde{\psi}^0(x) f_{GD}(x)/\psi^0$. On both figures, black crosses represent the normalized spectrum of $\overline{\partial_t \eta_l}(x)$. For interpretation, we expand weighted Doppler equation (33)

$$\begin{aligned}\frac{\widetilde{\psi}^0(x) f_{GD}(x)}{(2\pi)^{-1}\psi^0} &= Q_z \overline{\partial_t \eta_l}(x) + Q_z \mathrm{mss}_{\mathrm{xt}} \overline{\partial_x \eta_l}(x) \frac{\partial^2_{\tan^2\theta}\psi^0}{\psi^0} \\ &+ Q_z \frac{\partial_{\tan\theta}\psi^0}{\psi^0} \mathrm{mss}_{\mathrm{xt}} \\ &+ Q_z \frac{\partial_{\tan\theta}\psi^0}{\psi^0} \overline{\partial_x \eta_l}(x) \overline{\partial_t \eta_l}(x) \qquad (34)\end{aligned}$$

In this equation (34), second line, we recognize the constant component of the mean Doppler shift, corrected by a negligible range dependent term in the third line. The first term, first line, is the main modulation component, directly proportional to the surface elevation velocity. A correcting second term appears, proportional to the curvature of the NRCS fall-off with incidence. This term is also modulated and controlled by the line-of-sight sea surface slopes. The amplitude and the sign of $\partial^2_{\tan^2\theta}\psi^0$ are depending on the incidence and on the sea surface conditions. For the chosen sea condition, this term vanishes around 8 degrees, leading to the exact superposition of the velocity spectrum and the weighted Doppler shift spectrum (see figure 7). For lower and higher incidences than this inversion zone, the modulation spectrum of the weighted Doppler exhibits higher and lower spectral slopes than the velocity spectrum.

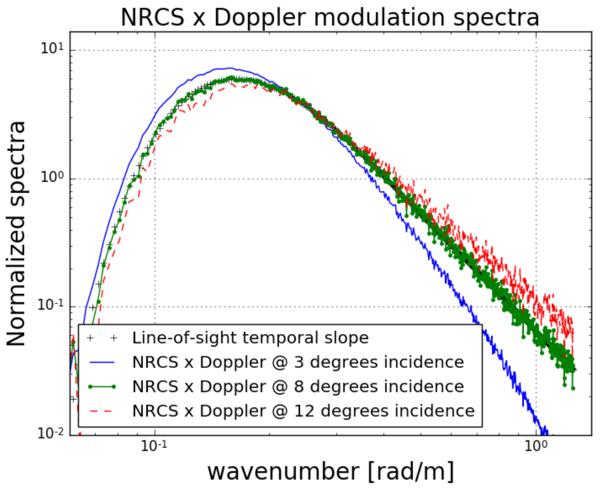

Fig. 7. Ka band - Normalized NRCS weighted Doppler modulation spectra at 3, 8 and 12 degrees incidence. Line-of-sight sea surface temporal slope ($\overline{\partial_t \eta}(x)$) spectra is also superimposed.

For open-ocean conditions, more complex sea state conditions are expected [9], likely leading to an higher incidence inversion zone. As such, a radar operating between 8 to 12 degree incidence represents an optimal configuration to best cancel out this curvature correction, and to help directly retrieve the surface velocity spectrum. As developed, range resolved measurements thus provide joint-directional information for both radar intensity and Doppler measurements, to uniquely characterize the ambient sea state, i.e directional spectral properties and kinematics.

IV. AIRSWOT DATA

The radar aboard AirSWOT (KaSPAR) is a Ka-band SAR sensor operated by NASA Jet Propulsion Laboratory (JPL) flying aboard a King Air B200 aircraft operated by NASA Armstrong Flight Research Center [21], [22]. The sensor gives

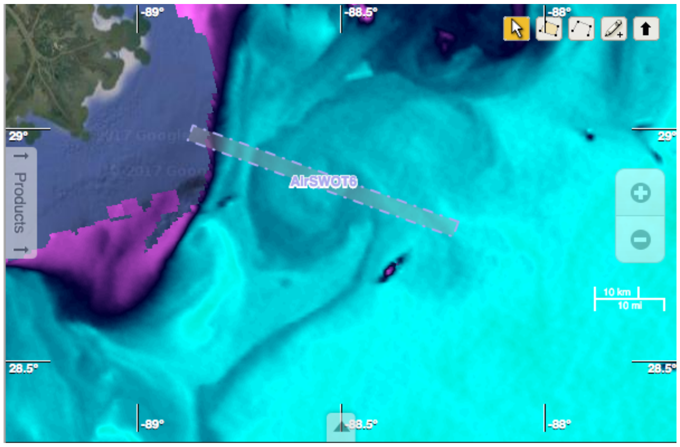

Fig. 8. AirSWOT flight #172803 on 2016/02/07 over the Hammer-Head mushroom seen by the VIIRS instrument (Sea Surface Temperature).

access to NRCS and Doppler maps over the illuminated scene which span from 0 to about 23 degrees incidence covering a distance of about 4 km in the range direction for the flights considered in this study. Both AirSWOT NRCS and SAR ATI Doppler data was processed and provided by NASA Jet Propulsion Laboratory. Figure 8 shows flight #172803 swath located over a "hammer-head" eddy, during the LASER experiment (LAgrangian Submesoscale ExpeRiment) [23], [24] conducted in the Gulf of Mexico in January and February 2016.

Figures 9 and 10 display radar intensity and Doppler maps sampled from the AirSWOT instrument, flight #172803 on February 7, 2017. Joint modulations are clearly detected, as expected from the previous developments. Ancillary data indicate surface wind speed of about 8 m.s^{-1}. Flight #172803 went from south-east to north-west, and the radar looked to the left, well aligned with the downwind/down-wave direction, as illustrated on figure 10. The detected peak wavelength of 45 m corresponds to short fetch conditions.

Figure 11 shows interpolated surface drifters velocity field at the time of the AirSWOT flight. Black lines are the swath boundaries. An along-track transect (red) of the AirSWOT Doppler map around the 12 degrees incidence is reported on figure 12 as well as the corresponding in-situ drifter velocity converted in line-of-sight equivalent Ka-band Doppler shift (top panel). A mean 83 Hz shift has been subtracted. The corresponding NRCS transect is also shown in the middle panel. The bottom panel shows the same drifter Doppler shift (-88 Hz) superimposed with the weighted Doppler shift $f_c \cdot \psi^0/\overline{\psi^0}$ where $\overline{\psi^0}$ is the mean magnitude of $\cos(12°)\sigma^0$ over the transect. The correspondence of the two measurements exemplify the sensibility of a 12 degrees incidence Ka-band Doppler radar to the sea surface current. Doppler and σ^0 range modulations can further be used to quantify this variability due to wave contribution and reduce current measurements uncertainties. This is presently outside the scope of this paper and left for further studies.

Figure 13.a shows the variation of AirSWOT Weighted Doppler (AS W.Doppler) as a function of incidence for 3 locations during flight #172803 (transects are reported on figure 11) with very different current velocities. These again demonstrate the sensitivity of the measurements to the current velocity. Figure 13.b shows equivalent Ka-band range Doppler shifts derived from the drifters surface velocities along the same three transects. Figure 13.c presents the difference of the first two panels and is the remaining wave Doppler bias. All curves are well superimposed for the three different transects and the local significant wave height variations (not shown here) explain, to first order, the remaining variability.

Finally, figure 14 shows the good correspondence of the NRCS spectrum, that is proportional to k^2 times the elevation spectrum $E(k)$, and the Doppler spectrum, proportional to

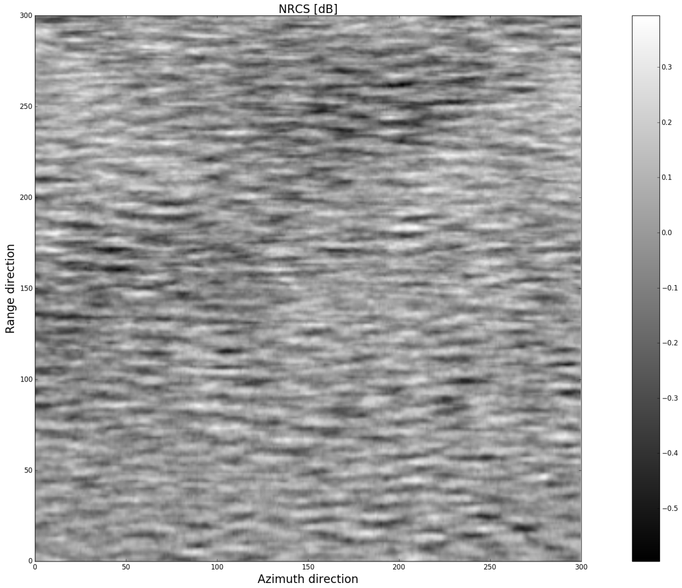

Fig. 9. Sample of NRCS modulations map observed with AirSWOT instrument on 2016/02/07 flight # 172803

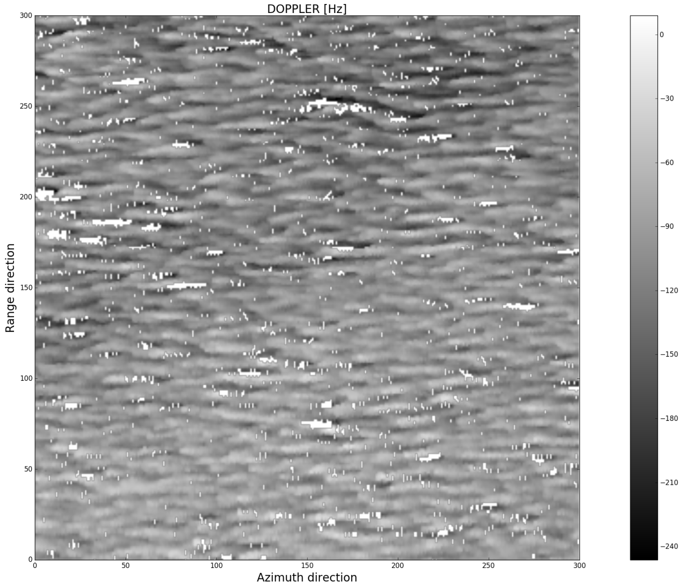

Fig. 10. Sample of Doppler modulations map observed with AirSWOT instrument on 2016/02/07 flight # 172803

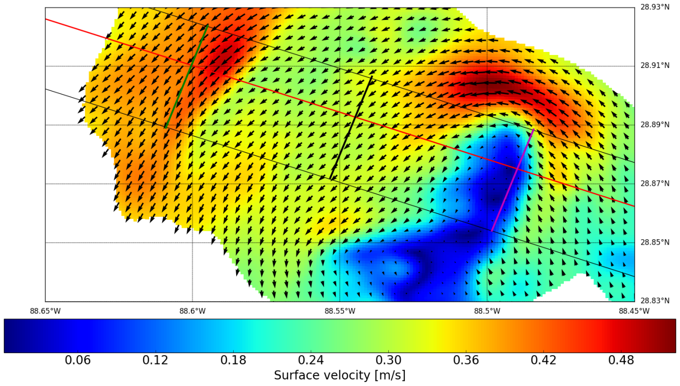

Fig. 11. Interpolated surface drifters velocity field colocated with AirSWOT flight # 172803 on 2016/02/07. Colors indicates the in-situ surface current velocity under the flight swath. Arrows indicates the surface current direction over the interpolated drifters area. Black lines are AirSWOT swath boundaries and red line is the 12 degrees incidence transect. Green, black and magenta range transects are shown figure 12 top panel.

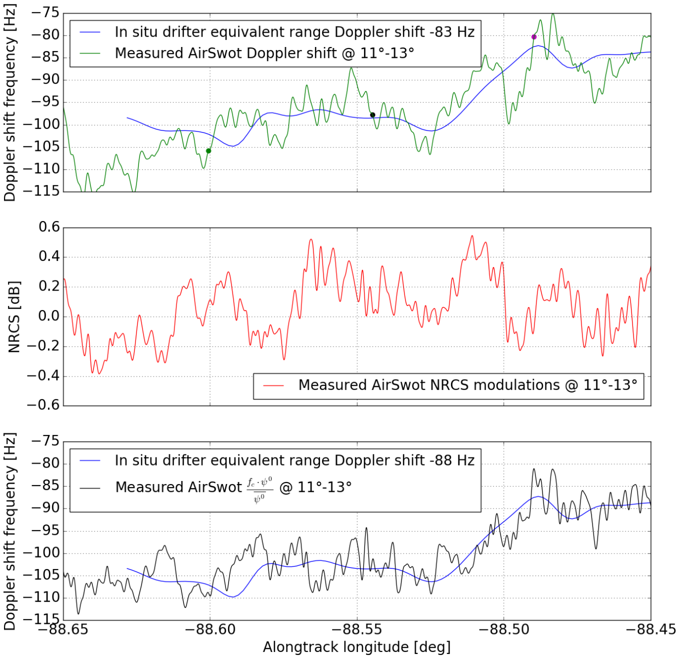

Fig. 12. Top panel: Transect of Ka Band Doppler shift estimated from drifter velocities and measured by AirSWOT around 12° incidence. Middle panel: Corresponding measured AirSWOT NRCS. Bottom panel: Measured NRCS-weighted Doppler shift. Data was gathered during AirSWOT flight # 172803 on 2016/02/07.

$kE(k)$ for deep water waves. Correspondence is particularly good around 12° incidence and consistent with our simple numerical test case in figure 7.

V. CONCLUSION

We have presented a theoretical framework for the analysis of Doppler near-nadir radars designed to sea surface velocities measurements. The Kirchhoff approximation is used to derive and understand the basic concepts of radar sensor physics. We focused on the SKIM satellite configuration which can operate in Ka-band at 6 and 12° incidence [5].

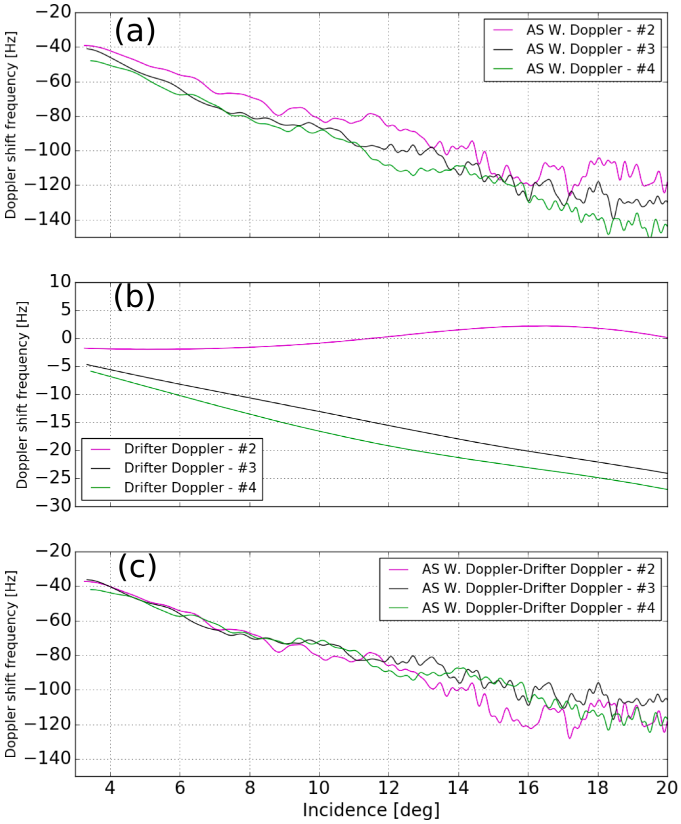

Fig. 13. (a) AirSWOT Weighted Doppler (AS W.Doppler) transects realized during flight #172803 and reported on figure 11. (b) In-situ drifter Ka-band equivalent range Doppler shifts. (c) Difference of the upper and middle panels. Remaining wave bias Doppler shifts of the three transects are superimposed meaning that wave conditions are similar.

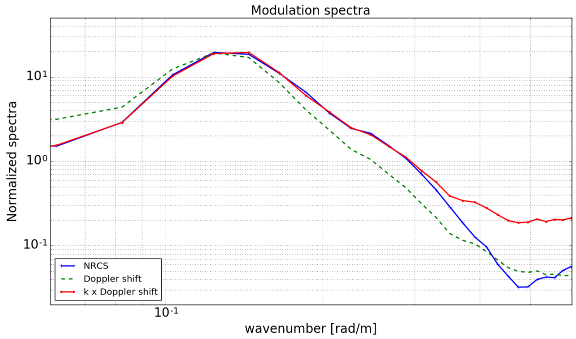

Fig. 14. AirSWOT range modulation NRCS and Doppler shift spectra. Modulation profiles between 11 and 13 degrees incidence only are considered and spectra are computed after a 400 m azimuthal averaging. The presented figure is the mean upwind spectra of AirSWOT flight # 172803 on 2016/02/07.

From these analytical developments, an important conclusion is that 12 degrees, in spite of a near-vertical geometry, is optimal for measuring time-varying waves in range-resolved measurements. This non-trivial conclusion comes from two results.

First, near-nadir configurations are favorable to infer directional wave properties (like CFOSAT). In particular, around 10-12 degrees incidence the NRCS second derivative with respect to incidence vanishes leading to linear relationships between the spectra of both NRCS and Doppler, and the spectrum of the sea surface elevation.

Second, up to 20 degrees incidence in Ka-band, the expected LOS velocity is largely dominated by the correlation between surface orbital velocities and slopes, the msv parameter (as also found from platform Ka-band radar measurements [25]). This LOS velocity can reach up to 50 times the inherent Stokes drift.

Hence, with a range resolution of 3 to 5 m when projected on the ground, the measured NRCS and Doppler modulation spectra can thus give an accurate estimation of the msv. It then allows to estimate and correct the large wave-induced bias in the Doppler velocity to infer the surface current [5]. For coarser range resolutions, typically 30 m and more, the estimation of the msv would be less accurate, and errors in retrieved surface currents larger.

These theoretical conclusions on the spectra of NRCS and Doppler and on the variation of the mean Doppler with incidence, wave and currents are confirmed by the analysis of AirSWOT data operating in Ka-band from 0 to 23 incidence. A particular attention was paid on flight #172803 realized on 2016/02/07 in downwind/downwave conditions. As obtained, σ^0 and Doppler shift range modulations are clearly visible. Measured Doppler shifts combined with ground truth surface current velocities derived from local drifters deployed during LASER experiments further confirm the expected current impact on time dependent measurements at near-nadir incidence.

This analysis clearly opens for new strategies to infer surface current information from precise ocean surface wave time-varying properties from satellite measurements.

VI. APPENDIX

A. Elevation, directional spectrum and correlation function

Without current, the linear random surface elevation η can be written:

$$\eta(\boldsymbol{r},t) = \int_{\mathbb{R}^2} \mathrm{d}\boldsymbol{k}\ a(\boldsymbol{k}) \mathrm{e}^{\mathrm{i}(\boldsymbol{k}\cdot\boldsymbol{r}-\omega t)} + c.c. \tag{35}$$

where $a(\boldsymbol{k})$ is half the complex wave amplitude of wave $\boldsymbol{k}$ with random phase and $c.c.$ being the complex conjugate. It rewrites:

$$\eta(\boldsymbol{r},t) = \int_{\mathbb{R}^2} \mathrm{d}\boldsymbol{k}\ \left[a(\boldsymbol{k})\mathrm{e}^{-\mathrm{i}\omega t} + a^*(-\boldsymbol{k})\mathrm{e}^{\mathrm{i}\omega t}\right] \mathrm{e}^{\mathrm{i}\boldsymbol{k}\cdot\boldsymbol{r}} \tag{36}$$

The cross-correlation $\rho(\boldsymbol{r}-\boldsymbol{r}', t-t') = \langle \eta(\boldsymbol{r},t)\eta(\boldsymbol{r}',t')\rangle$ writes

$$\rho(\boldsymbol{\xi},\tau) = \int_{\mathbb{R}^2} d\boldsymbol{k} \left[S_d(\boldsymbol{k})\mathrm{e}^{-\mathrm{i}\omega\tau} + S_d^*(-\boldsymbol{k})\mathrm{e}^{\mathrm{i}\omega\tau}\right] \mathrm{e}^{\mathrm{i}\boldsymbol{k}\cdot\boldsymbol{\xi}} \tag{37}$$

where $S_d(\boldsymbol{k})$ defined by $\langle a(\boldsymbol{k})a^*(\boldsymbol{k}')\rangle = S_d(\boldsymbol{k})\delta(\boldsymbol{k}-\boldsymbol{k}')$ is half the square amplitude of wave $\boldsymbol{k}$ and is real.

Note that S_d is the directive oceanic spectrum which is not centro-symmetric. It follows that:

$$S(\boldsymbol{k}) = S_d(\boldsymbol{k}) + S_d(-\boldsymbol{k}) \tag{38}$$

is the well known centro-symmetric spectrum.

Adding a horizontal current $\boldsymbol{U}$, (equation (20)), we get

$$\eta_c(\boldsymbol{r},t) = \int_{\mathbb{R}^2} d\boldsymbol{k}\ \left[a(\boldsymbol{k})\mathrm{e}^{-\mathrm{i}\omega t} + a^*(-\boldsymbol{k})\mathrm{e}^{\mathrm{i}\omega t}\right] \mathrm{e}^{\mathrm{i}\boldsymbol{k}\cdot(\boldsymbol{r}-\boldsymbol{U}t)} \tag{39}$$

where subscript $_c$ accounts for current. The cross-correlation $\rho_c(\boldsymbol{r}-\boldsymbol{r}', t-t') = \langle \eta_c(\boldsymbol{r},t)\eta_c(\boldsymbol{r}',t')\rangle$ writes

$$\rho_c(\boldsymbol{\xi},\tau) = \int_{\mathbb{R}^2} d\boldsymbol{k} \left[S_d(\boldsymbol{k})\mathrm{e}^{-\mathrm{i}\omega\tau} + S_d^*(-\boldsymbol{k})\mathrm{e}^{\mathrm{i}\omega\tau}\right] \mathrm{e}^{\mathrm{i}\boldsymbol{k}\cdot(\boldsymbol{\xi}-\boldsymbol{U}\tau)}, \tag{40}$$

and we recognize

$$\rho_c(\boldsymbol{\xi},\tau) = \rho(\boldsymbol{\xi}-\boldsymbol{U}\tau,\tau). \tag{41}$$

B. Residual modulation statistics

Let us denotes by $(x,y) \mapsto f(x,y)$ the random function of interest, e.g. sea surface elevation, slope, velocity, and/or radar reflectivity modulation, with l_x and l_y, the correlation lengths along x and y, respectively, and $D = [-L_x/2, L_x/2] \times [-L_y/2, L_y/2]$ the bounded 2D intercepted domain. We also denote by

$$m_y(x) = \frac{1}{L_y}\int_{-\frac{L_y}{2}}^{\frac{L_y}{2}} dy\ f(x,y), \tag{42}$$

the residual, along y, mean profile of interest and

$$m = \frac{1}{L_x L_y}\iint_D dxdy\ f(x,y) \tag{43}$$

the mean of f. We assume that $l_x \ll L_x$ and also that f is smooth and homogeneous. Accordingly, the covariance of f for $x-x'=0$ becomes $C\left(0,(y-y')/l_y\right)$ and is evaluated as

$$\frac{1}{L_x}\int_{-\frac{L_x}{2}}^{\frac{L_x}{2}} dx\left(f(x,y)-m_x(y)\right)\left(f(x,y')-m_x(y')\right)^\star \tag{44}$$

with

$$m_x(y) = \frac{1}{L_x}\int_{-\frac{L_x}{2}}^{\frac{L_x}{2}} dx'\ f(x',y). \tag{45}$$

Then, the variance of the residual modulation writes:

$$\begin{aligned}
V &= \frac{1}{L_x}\int_{-\frac{L_x}{2}}^{\frac{L_x}{2}} dx\ |m_y(x)-m|^2 \\
&= \frac{1}{L_x}\int_{-\frac{L_x}{2}}^{\frac{L_x}{2}} dx\ \left|\frac{1}{L_y}\int_{-\frac{L_y}{2}}^{\frac{L_y}{2}} dy\ \left(f(x,y)-m_x(y)\right)\right|^2 \\
&= \frac{1}{L_y^2}\int_{\left[-\frac{L_y}{2},\frac{L_y}{2}\right]^2} dydy'\ C\left(0,\frac{y-y'}{l_y}\right), \\
&= \frac{l_y^2}{2L_y^2}\int_{-\frac{L_y}{l_y}}^{\frac{L_y}{l_y}} d\Delta y\int_{-(\frac{L_y}{l_y}-|\Delta y|)}^{\frac{L_y}{l_y}-|\Delta y|} dy_c\ C\left(0,\Delta y\right) \\
&\quad \text{with}\quad \Delta y = \frac{y-y'}{l_y}\ \text{and}\ y_c = \frac{y+y'}{l_y}, \\
&= \left(\frac{l_y}{L_y}\right)^2\int_{-\frac{L_y}{l_y}}^{\frac{L_y}{l_y}} d\Delta y\ \left(\frac{L_y}{l_y}-|\Delta y|\right) C\left(0,\Delta y\right)
\end{aligned} \tag{46}$$

This general expression can then be analytically evaluated for specific covariance functions (e.g. Gaussian covariance). For the asymptotic case $l_y \ll L_y$, $(L_y/l_y - |\Delta y|) \approx L_y/l_y$ for bounded $|\Delta y|$. At large $|\Delta y|$, $C(0, \Delta y)$ rapidly decreases, leading to

$$V \approx \left(\frac{l_y}{L_y}\right) \int_{-\infty}^{\infty} d\Delta y \; C(0, \Delta y) . \tag{47}$$

Depending on their directional covariance properties, i.e. distributed spectral directional spreads governing l_y, residual modulations thus further decreases with the azimuthal extent of the intercepted domain L_y. This development generalizes previous analyses [10], explicitly introducing the previously omitted, l_y dependency.

ACKNOWLEDGMENT

This work was supported by CNES under the SWOT preparation program and LabexMer via grant ANR-10-LABX-19-01. The authors would like to thank NASA Jet Propulsion Laboratory and in particular Xiaoqing Wu for processing the AirSWOT data and Ernesto Rodriguez for discussions and provision of the data. The interpolated LASER drifter velocity field was provided by Rafael Goncalves at RSMAS. Part of the research was carried out at the Jet Propulsion Laboratory, California Institute of Technology, under a contract with the National Aeronautics and Space Administration (NASA).

REFERENCES

[1] B. Chapron, F. Collard, and F. Ardhuin, “Direct measurements of ocean surface velocity from space: interpretation and validation,” *J. Geophys. Res.*, vol. 110, no. C07008, 2005.

[2] A. Mouche, B. Chapron, N. Reul, and F. Collard, “Predicted doppler shifts induced by ocean surface wave displacements using asymptotic electromagnetic wave scattering theories,” *Waves in Random and Complex Media*, vol. 18, no. 1, pp. 185–196, 2008.

[3] F. Nouguier, C.-A. Guérin, and G. Soriano, “Analytical techniques for the doppler signature of sea surfaces in the microwave regime-i: Linear surfaces,” *IEEE Transactions on Geoscience and Remote Sensing*, vol. 49, no. 12, pp. 4856–4864, 2011.

[4] G. Caudal, D. Hauser, R. Valentin, and C. Le Gac, “Kuros: A new airborne ku-band doppler radar for observation of surfaces,” *Journal of Atmospheric and Oceanic Technology*, vol. 31, no. 10, pp. 2223–2245, 2014.

[5] F. Ardhuin, Y. Aksenov, A. Benetazzo, L. Bertino, P. Brandt, E. Caubet, B. Chapron, F. Collard, S. Cravatte, F. Dias, G. Dibarboure, L. Gaultier, J. Johannessen, A. Korosov, G. Manucharyan, D. Menemenlis, M. Menendez, G. Monnier, A. Mouche, F. Nouguier, G. Nurser, P. Rampal, A. Reniers, E. Rodriguez, J. Stopa, C. Tison, M. Tissier, C. Ubelmann, E. van Sebille, J. Vialard, and J. Xie, “Measuring currents, ice drift, and waves from space: the sea surface kinematics multiscale monitoring (skim) concept,” *Ocean Sci. Discuss.*, 2017.

[6] M. Hansen, V. Kudryavtsev, B. Chapron, J. Johannessen, F. Collard, K.-F. Dagestad, and A. Mouche, “Simulation of radar backscatter and doppler shifts of wave–current interaction in the presence of strong tidal current,” *Remote sensing of environment*, vol. 120, pp. 113–122, 2012.

[7] R. Romeiser, H. Runge, S. Suchandt, R. Kahle, C. Rossi, and P. S. Bell, “Quality assessment of surface current fields from terrasar-x and tandem-x along-track interferometry and doppler centroid analysis,” *IEEE Transactions on Geoscience and Remote Sensing*, vol. 52, no. 5, pp. 2759–2772, 2014.

[8] A. C. Martin, C. Gommenginger, J. Marquez, S. Doody, V. Navarro, and C. Buck, “Wind-wave-induced velocity in ati sar ocean surface currents: First experimental evidence from an airborne campaign,” *Journal of Geophysical Research: Oceans*, vol. 121, no. 3, pp. 1640–1653, 2016.

[9] F. Nouguier, A. Mouche, N. Rascle, B. Chapron, and D. Vandemark, “Analysis of dual-frequency ocean backscatter measurements at ku-and ka-bands using near-nadir incidence gpm radar data,” *Ieee Geoscience And Remote Sensing Letters*, vol. 13, no. 9, pp. 1310–1314, 2016.

[10] F. C. Jackson, “An analysis of short pulse and dual frequency radar techniques for measuring ocean wave spectra from satellites. 1981,” *Radio Science*, vol. 16, no. 6, pp. 1385–1400.

[11] ——, “The radar ocean-wave spectrometer,” *Johns Hopkins APL Technical Digest*, vol. 8, pp. 116–127, 1987.

[12] D. Hauser, C. Tison, T. Amiot, L. Delaye, N. Corcoral, and P. Castillan, “SWIM: The first spaceborne wave scatterometer,” *IEEE Trans. on Geosci. and Remote Sensing*, vol. 55, no. 5, pp. 3000–3014, 2017.

[13] D. Thompson, B. Gotwols, and W. Keller, “A comparison of ku-band doppler measurements at 20° incidence with predictions from a time-dependent scattering model,” *Journal of Geophysical Research: Oceans*, vol. 96, no. C3, pp. 4947–4955, 1991.

[14] T. Elfouhaily, B. Chapron, K. Katsaros, and D. Vandemark, “A unified directional spectrum for long and short wind-driven waves,” *Journal of Geophysical Research: Oceans*, vol. 102, no. C7, pp. 15 781–15 796, 1997.

[15] E. Walsh, C. Wright, M. Banner, D. Vandemark, B. Chapron, J. Jensen, and S. Lee, “The southern ocean waves experiment. part iii: Sea surface slope statistics and near-nadir remote sensing,” *Journal of physical oceanography*, vol. 38, no. 3, pp. 670–685, 2008.

[16] J. A. Johannessen, B. Chapron, F. Collard, V. Kudryavtsev, A. Mouche, D. Akimov, and K.-F. Dagestad, “Direct ocean surface velocity measurements from space: Improved quantitative interpretation of envisat asar observations,” *Geophysical Research Letters*, vol. 35, no. 22, 2008.

[17] M. J. Rouault, A. Mouche, F. Collard, J. A. Johannessen, and B. Chapron, “Mapping the agulhas current from space: An assessment of ASAR surface current velocities,” *J. Geophys. Res.*, vol. 41, p. C10026, 2010.

[18] A. A. Mouche, F. Collard, B. Chapron, K.-F. Dagestad, G. Guitton, J. A. Johannessen, V. Kerbaol, and M. W. Hansen, “On the use of doppler shift for sea surface wind retrieval from sar,” *IEEE Transactions on Geoscience and Remote Sensing*, vol. 50, no. 7, pp. 2901–2909, 2012.

[19] F. Nouguier, C.-A. Guérin, and B. Chapron, ““choppy wave” model for nonlinear gravity waves,” *Journal of Geophysical Research: Oceans*, vol. 114, no. C9, 2009.

[20] F. C. Jackson, “The reflection of impulses from a nonlinear random sea,” *Radio Science*, vol. 16, no. 6, pp. 1385–1400, 1981.

[21] “Airswot description,” https://swot.jpl.nasa.gov/airswot/.

[22] D. Moller, E. Rodriguez, J. Carswell, and D. Esteban-Fernandez, “Airswot-a calibration/validation platform for the swot mission,” in *Proc. Interntational Geoscience and Remote Sensing Symposium, Vancouver, Canada*, July 2011.

[23] E. H. Altenau, T. M. Pavelsky, D. Moller, C. Lion, L. H. Pitcher, G. H. Allen, P. D. Bates, S. Calmant, M. Durand, and L. C. Smith, “Airswot measurements of river water surface elevation and slope: Tanana river, ak,” *Geophysical Research Letters*, vol. 44, no. 1, pp. 181–189, 2017.

[24] R. Lumpkin, T. Özgökmen, and L. Centurioni, “Advances in the application of surface drifters,” *Annu. Rev. Mar. Sci.*, vol. 9, pp. 6.1–6.23, 2017.

[25] Y. Y. Yurovsky, V. N. Kudryavtsev, S. A. Grodsky, and B. Chapron, “Normalized radar backscattering cross-section and doppler shifts of the sea surface in ka-band,” *submitted*, 2017.

Frédéric Nouguier received the ´Agrégation” and the M.S. degrees in applied physics from the Ecole Normale Supérieure de Cachan, France, the M.S. degree in physical methods for remote sensing from the University of Paris-Diderot, Paris and the Ph.D. degree in physics from the University of Marseille, France, in 2009. He is now a Research Scientist at the Laboratoire d'Océanographie Physique et Spatiale (LOPS), IFREMER, Plouzané, France. He has experience in applied mathematics, physical oceanography, and electromagnetic wave theory and its application to ocean remote sensing.

Bertrand Chapron received the B.Eng. degree from the Institut National Polytechnique de Grenoble, Grenoble, France, in 1984 and the Ph.D. degree in physics (fluid mechanics) from the University of Aix-Marseille II, Marseille, France, in 1988. He spent three years as a Postdoctoral Research Associate with the NASA Goddard Space Flight Center, Greenbelt, MD, and the Wallops Flight Facility, Wallops Island, VA. He is a Research Scientist at the Laboratoire d'Océanographie Physique et Spatiale (LOPS), Institut Francais de Recherche et d'Exploitation de la Mer (IFREMER), Plouzané, France. He has experience in applied mathematics, physical oceanography, and electromagnetic wave theory and its application to ocean remote sensing.

Fabrice Collard graduated from the Ecole Centrale de Lyon in 1996, where he studied off-shore engineering. In 2000, he received the Ph.D. in Oceanography, Meteorology and Environment from University of Paris VI. His thesis was dedicated to the three dimensional aspect of wind-wave field. He spent two years as a post-doctoral research associate working on HF radars at RSMAS, Miami, USA (2000-2001). He spent one year at the Oceanography from Space Laboratory, IFREMER, France (2002),working on the validation of the synthetic aperture radar Wave mode products of ENVISAT. He has been research engineer at BOOST-Technologies (2003/2008) and head of R&D activities at the Radar Application Division of CLS (2008-2013), working on the development of algorithms and prototypes for operational wind wave and current applications. He is now president of OceanDataLab, working on ocean remote sensing multi-sensor synergy methods and tools.

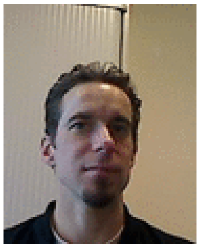

Alexis A. Mouche received the Ph.D. degree in ocean remote sensing in 2005 at the Universit'e de Versailles Saint-Quentin, France. He has a permanent position with the Laboratoire d'Océanographie Physique et Spatiale, Institut Francais de Recherche pour l'Exploitation de la Mer, Plouzané, France, since January 2014. His principal field of interest is the interaction of electromagnetic and oceanic waves for ocean remote sensing applications.

Nicolas Rascle graduated from ENSTA (Paris, France) in 2004. He received his Ph.D. degree in 2007 at UBO (Brest, France). He spent 3 years as a postdoctoral research associate at UCT (Cape Town, South Africa). He worked as a research associate at IFREMER (Brest, France) from 2012 to 2017. He is specialized in wave dynamics. He mainly worked on the impact of waves on the air-sea interface (turbulence, surface currents, wave-current interactions). He is also specialized on the role of waves and surface roughness for the remote sensing of wind, waves and currents.

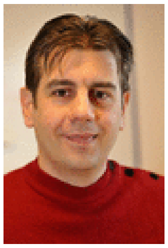

Fabrice Ardhuin graduated from Ecole Polytechnique, Palaiseau, France, in 1997 and received the Ph.D. degree in oceanography at the U.S.Naval Postgraduate School, Monterey, CA, in 2001. He has been working on ocean waves and related topics, from microseisms to remote sensing, with a strong focus on wave-current and wave-ice interactions, first at the French Navy Hydrographic and Oceanographic Service (SHOM), then Ifremer, and now CNRS. He is now the chairman of LOPS, member of the SWOT science team, and PI for the SKIM proposal.

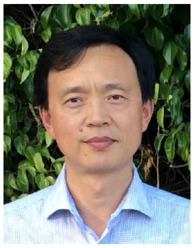

Xiaoqing Wu received the B.S. and M.S. degrees in electrical engineering from Nanjing University of Aeronatics and Astronautics, Nanjing, China, in 1982 and 1985, respectively, and Ph.D. in electrical engineering from the University of Stuttgart, Stuttgart, Germany, in 1998. He was involved in data system design and development for the Modified Antarctic Mapping Mission and contributed to producing the first Antarctic surface velocity map and the interferometric coherence map while he worked from 1998 to 2008 as a Senior Research Engineer with Vexcel Corporation, Boulder, CO, where he has been involved in radar ice sounding since 2005. He joined the Jet Propulsion Laboratory, California Institute of Technology, Pasadena, in 2008 and has produced the first radar image of Greenland ice sheet bed. He has been also involved in NASA's SWOT mission, Glistin and AirSWOT projects with extensive experiences in SAR data processing and analysis. His research interests include synthetic aperture radar (SAR) processing algorithms, interferometry, SAR tomography, and radar ice sounding.